Journal of Inorganic Biochemistry 197 (2019) 110697

Contents lists available at ScienceDirect

Journal of Inorganic Biochemistry

journal homepage: www.elsevier.com/locate/jinorgbio

Effect of the point mutation H54N on the ferroxidase process of *Rana catesbeiana* H′ ferritin

Cecilia Pozzi[a], Flavio Di Pisa[a], Daniela Lalli[b], Camilla Rosa[b], Paola Turano[b,c], Stefano Mangani[a,b,*]

[a] Department of Biotechnology, Chemistry and Pharmacy, Department of Excellence 2018–2020, University of Siena, via Aldo Moro, 2, 53110 Siena, Italy
[b] Magnetic Resonance Center CERM, University of Florence, via Luigi Sacconi, 6, 50019 Sesto Fiorentino, FI, Italy
[c] Department of Chemistry, Department of Excellence 2018–2020, University of Florence, via della Lastruccia 2, 50019 Sesto Fiorentino, FI, Italy

ARTICLE INFO

Keywords:
H′ ferritin
X-ray anomalous diffraction
Iron
Reaction mechanism
Iron storage

ABSTRACT

Human H and *Rana catesbeiana* H′ subunits in vertebrate ferritin protein cages catalyze the Fe(II) oxidation by molecular oxygen and promote the ferric oxide biomineral synthesis. By depositing iron biomineral, ferritins also prevent potentially toxic reactions products from Fe(II)-based Fenton chemistry. Recent work from our laboratory was aimed to describe the iron pathways within ferritin, from entrance into the cage to the ferroxidase site, and to understand the role played by amino-acid residues in iron trafficking and catalysis. Our approach exploits anomalous X-ray diffraction from ferritin crystals, exposed to a ferrous salt, to track transient iron binding sites along the path towards a well-defined di-iron site where they get oxidized by oxygen. Coupling structure determination with solution kinetic measurements on selected variants, allows validating the role played by key residues on the catalytic iron oxidation. Our previous studies on H′ ferritin indicated the regulatory role played by His54, and by its human counterpart Gln58, on guiding Fe(II) ions to the catalytic site. Here, we have investigated the effects induced by substituting the wild type His54 with Asn54, having different iron coordination properties. We have obtained a series of atomic-resolution crystal structures that provide time-dependent snapshots of iron bound at different locations in the H′ ferritin H54N variant. The comparison with H′ ferritin and H′ ferritin H54Q variant leads to identify a new iron binding site. Our kinetic and structural data support the role of H′ ferritin residue 54 in regulating the access of Fe(II) ions to the catalytic site.

1. Introduction

Ferritins are ubiquitous nanocage proteins involved in iron homeostasis. Iron is stored and concentrated within the central cavity of ferritins in the form of a hydrated ferric oxide biomineral (up to 4500 iron ions can be stored inside a single cage in vitro). Furthermore, ferritins also function as antioxidants by retrieving iron ions released subsequently to the degradation of iron-proteins, thus preventing the occurrence of Fenton-like chemistry [1].

Ferritins are characterized by a quaternary structure generated by the self-assembly of 24 protein subunits into a hollow nanocage having an outer diameter of approximately 120 Å and an internal cavity of about 80 Å across [2,3]. The quaternary structure of maxi-ferritins is marked by a 432 point symmetry with three four-fold, four three-fold, and six two-fold symmetry axes. In vertebrates, ferritin is an hetero-oligomeric complex composed of two different types of chains, classified according to their respective molecular weight in L (light) and H (heavy) [1,4]. H chains are deputed to ferroxidase activity, relaying on the catalytic oxidation of Fe(II) to Fe(III) in the presence of di-oxygen, performed at the so-called ferroxidase center [1]. L-type chains do not possess the catalytic ferroxidase site but they are involved in the biomineralization reaction through a nucleation site, located on the internal cage surface, in which iron atoms assemble to form trinuclear iron(III) clusters [5]. Amphibians have a third type of subunits, called M (middle) or H′, sharing 64% sequence homology with the human H chain.

The catalytic oxidation reaction occurring at the ferroxidase sites in eukaryotic ferritins occurs in vitro on the ms time scale and can be monitored by following the formation and decay of the differic peroxo intermediate at 650 nm and the formation of ferric-oxo product at 350 nm [6]. The reaction rate is modulated by the nature of residues inside the channels connecting the bulk solution to the inner cavity in

* Corresponding author at: Department of Biotechnology, Chemistry and Pharmacy, University of Siena, via Aldo Moro, 2, 53110 Siena, Italy.
E-mail addresses: pozzi4@unisi.it (C. Pozzi), flavio.dipisa@unisi.it (F. Di Pisa), camilla.rosa@meyer.it (C. Rosa), turano@cerm.unifi.it (P. Turano), stefano.mangani@unisi.it (S. Mangani).

https://doi.org/10.1016/j.jinorgbio.2019.110697
Received 14 December 2018; Received in revised form 23 April 2019; Accepted 24 April 2019
Available online 07 May 2019
0162-0134/

correspondence to the three-fold symmetry axes. Substitution of carboxylate residues at the interior channel exits drastically inhibits the catalytic ferroxidase reaction, which has led to the identification of the three-fold channels as the iron ion entry channels [7,8].

During the last years, we have developed a crystallographic approach to monitor the transient iron binding sites in the ferritin nanocage, which relies on solid-to-solid diffusion of iron ions from crystalline Mohr's salt (salt grains added directly to the crystallization drops containing preformed protein crystals) [9,10]. The crystal-to crystal diffusion is relatively generated by and iron loading can be stopped by flash-freezing the ferritin crystals in liquid nitrogen after controlled times in the range 1–120 min of free diffusion, before crystals begin to deteriorate. Ferritin crystals of high diffraction quality can be obtained using molar concentrations of $MgCl_2$ as precipitant. The incoming Fe(II) ions compete with Mg(II) ions already bound to several protein sites along the substrate pathway so that the bound Mg(II) ions contribute to further slowing down the iron oxidation reaction at the ferroxidase site [9,10].

The time-controlled iron-loading experiments allowed us to identify a number of iron sites, which populated progressively as the iron loading time increases. The functional relevance of these sites has been verified by mutating the amino acids observed to interact with iron into residues with different chemical properties and then by monitoring the effect of the mutation on the reaction kinetics in solution [9–13].

Over the selected time frame for iron diffusion in the ferritin crystals, we consistently detect a series of iron binding events that follow a well-defined order in both *Rana catesbeiana* H′ ferritin (*Rc*H′f) and human H ferritin (HuHf) [9,10]. The first iron ion appears at the ferroxidase center, coordinated by Glu23, His61 and Glu58. This is the so-called Fe1 site and represents the highest iron affinity site in vertebrate ferritins. This crystallographic result is fully consistent with thermodynamic data [14]. The population of the dinuclear site is completed by the binding of a second iron ion at the Fe2 site, where Fe(II) is coordinated by Glu103, as bidentate ligand, and by Glu58, which bridges it to Fe1. The coordination sphere of Fe1and Fe2 is completed by water molecules.

Additional iron binding sites, called accessory sites, in the close proximity of the ferroxidase center are then populated. Their exact location and number are protein-dependent. In *Rc*H′f (PDB: 4MY7) and in *Rc*H′f H54Q variant (PDB: 4MN9) the accessory iron sites, Fe3, Fe4 and Fe5, are found. Fe3 coordination is given by His54 (Gln54 in the H54Q variant), Glu57 (monodentate), Glu103 (monodentate), Asp140 (monodentate) and completed by two water molecules. Fe4 is bound to Glu57 (bidentate), Asp140 (bidentate), one water molecule in the basal plane and by Glu136 (monodentate) and a second water molecule as axial ligands. A further Fe site is found in the H54Q variant, where Fe (II) is bound to Glu53 (monodentate), Glu57 (monodentate) and four water molecules [9]. In HuHf (PDB: 4ZJK) the Fe3 and Fe4 sites are different from those of *Rc*H′f [10]. The role of these accessory sites was studied in a *Rc*H′f variant in which Glu57, Glu136 and Asp140 were replaced by alanine residues through site directed mutagenesis and they were proven to play a fundamental role in promoting an efficient reaction turnover [11]. The Fe3, Fe4 and Fe5 sites are increasingly distant from the catalytic center. The arrangement of the iron sites and their binding order suggest the existence of a multistep iron pathway leading to the ferroxidase site under the guidance of an array of transiently and weakly coordinating sites [9,10]. Finally, two hexa-aqua iron ions are observed inside the threefold channels, where they have second coordination sphere interactions with symmetry related Asp127 and Glu130, respectively. They have been interpreted as ferrous ions diffusing into the nanocavity through the ion channels thanks to the attractive driving force created by an increasingly negative electrostatic gradient across these hydrophilic channels [11,15,16].

The series of iron binding sites observed via time-lapse crystallography provides a picture of the iron uptake process by the ferritin cage along a backward path where the first sites to be populated are those in the ferroxidase center, followed by accessory sites at the interface between the ferroxidase center and the inner cavity, and finally by the ion entry channels. Iron accumulates along the path because of the hindered turnover in the crystal. As the iron(II) ions approach the ferroxidase centers they get progressively dehydrated, with water ligands replaced by protein amino acids.

The differences in the position and number of the accessory iron binding sites along this path in *Rc*H′f and HuHf are reflected in their different reaction rates [9,10]. In HuHf, Gln58 replaces *Rc*H′f His54. Our study about the H54Q variant of *Rc*H′f demonstrated that changing this residue modulates the distribution of accessory iron binding sites [9].

Here, we report the functional and structural characterization of the *Rc*H′f variant H54N, generated to test the effect of shortening of the side chain of this residue, while maintaining the same coordination abilities as in the H54Q variant. A series of high-resolution anomalous diffraction experiments was performed on single protein crystals of *Rc*H′f H54N exposed to ferrous ions for various time intervals under aerobic conditions. These results provide direct analysis of Fe(II) binding in the protein as well as detailed information on the identity of the transient iron binding sites populated along the pathway from the cage entry channels at the three-fold axes to the ferroxidase sites.

2. Experimental section

2.1. Mutagenesis

The plasmid pET3a carrying the *Rc*H′f ferritin gene was used for introducing the H54N mutation. Primers for mutation were designed with the web-based software PrimerX (http://bioinformatics.org/primerx/). Site directed amino acid substitutions in *Rc*H′f ferritin were generated by polymerase chain reaction (PCR), with the expression plasmid pET-3a *Rc*H′f DNA as the template, following previously reported protocols [9,17]. Gene sequencing was done to confirm the mutations (Primm srl, Milan, Italy).

2.2. Recombinant expression and purification of R. catesbeiana H′ ferritin variant H54N

*Rc*H′f ferritin was expressed and purified using adapted protocols from the literature [18]. *E. coli* BL21(DE3) pLysS cells containing the mutated plasmid DNA were cultured in rich media (Luria Broth) and grown at 37 °C and 180 rpm until OD_{600} reached 0.7. The expression started after addition of isopropyl β-D-1-thiogalactopyranoside (IPTG; 1 mM final concentration), and the culture was incubated for 4 h. After harvesting by centrifugation, the cells were lysed using lysozyme and sonication. In order to purify ferritin, coagulation of temperature-sensitive proteins and two chromatography steps were involved. First, the supernatant of the centrifuged lysate was heated at 65 °C for 15 min and the aggregated proteins were sedimented by ultracentrifugation (40 min, 40,000 rpm, 4 °C). Then, the supernatant was dialyzed against 20 mM Tris buffer, pH 7.5. Finally, the sample was loaded onto a 120 mL sulphopropyl (SP) Sepharose anion-exchange column (GE Healthcare, Sweden) and eluted with a linear NaCl gradient (0–1 M) in 20 mM Tris buffer, pH 7.5. Pertinent fractions were determined by sodium dodecyl sulphate - polyacrylamide gel electrophoresis (SDS-PAGE), and those containing ferritin were concentrated using an Amicon ultracentrifugal filter device with a molecular weight cutoff of 14 kDa (Millipore, U.S.A.). The sample was then loaded onto a 120 mL dextran size exclusion column and eluted with 20 mM Tris buffer, pH 7.5. Fractions were monitored by UV–vis spectroscopy and pooled together to obtain a final ferritin sample. The sample was then demineralized through several steps of dialysis: 4 dialysis at room temperature against 2 L 20 mM Tris pH 7.5, 5 mL 500 mM EDTA pH 5.8, 10 mL ammonium thioglycolate, to reduce and chelate iron, and 4 dialysis at room temperatures against 2 L 20 mM Tris pH 7.5 to remove

the chelated ion from the ferritin core. The maintenance of the typical quaternary structure of the ferritin 24-mer was demonstrated by size exclusion chromatography, which shows an elution chromatograms (UV measure) superimposable to that of the wild type protein.

2.3. Stopped-flow kinetics on RcH′f variant H54N

The kinetics of iron uptake by the H54N apoferritin variant was monitored as the change in absorbance at 650 nm (diferric peroxo, DFP, intermediate) or at 350 nm ($[Fe^{3+}O]_n$ products). Measurements were carried out using a UV/visible, stopped-flow spectrometer (model SX-18 MV) Applied Photophysics (U.K.). Absorbance curves were measured after mixing equal volumes of 100 μM protein subunits in 200 mM MOPS, 200 mM NaCl, pH 7.0 buffer, with a freshly prepared solution of 200 μM ferrous sulphate in 1 mM HCl, in order to obtain a 2 Fe/subunit (i.e., 48 Fe/nanocage) complex. 4000 data points were collected during 10 s. Initial rates of diferric peroxide (DFP) reaction intermediate and $[Fe^{3+}O]_n$ species formation were determined from the fitting of the linear portion of the absorbance curves recorded at 650 nm and 350 nm, respectively. The data are averages of a set of 3 experiments.

2.4. Crystallization of RcH′f variant H54N

Crystals of *Rc*H′f variant H54N were grown using the hanging-drop vapor-diffusion method at 8 °C. Drops were prepared by mixing equal volumes of metal-free *Rc*H′f variant H54N (7–14 mg mL^{-1} in 20 mM Tris-HCl pH 7.5) and precipitant (1.6–2.0 M $MgCl_2{\cdot}6\ H_2O$, 0.1 M bicine pH 9) solutions and equilibrated over 600 μL reservoir. Octahedral crystals appeared in 1–3 days and grew to final dimensions of 200–800 μm within one week. The time-controlled iron-loading study was performed on *Rc*H′f H54N crystals under aerobic conditions by free iron diffusion from solid Mohr's salt $[(NH_4)_2Fe(SO_4)_2{\cdot}6\ H_2O]$ [9]. Crystals of Mohr's salt were added directly into the crystallization drop containing preformed protein crystals and iron loading was stopped after the controlled times of 2, 15 and 60 min by flash-freezing *Rc*H′f H54N crystals directly in liquid nitrogen, according to a well-established procedure already adopted for wild-type (wt) *Rc*H′f and its variant H54N.

2.5. Data collection, structure solution and refinement

X-ray crystallographic data were collected using synchrotron radiation at the European Synchrotron Radiation Facility (ESRF, Grenoble, France) beamline BM14, equipped with a MARmosaic 225 detector, and at the Elettra (Trieste, Italy) beamline XRD1, equipped with a Dectris Pilatus 2M detector. Data were integrated using either Mosflm [19] or XDS [20] and scaled with Scala [21] from the CCP4 suite [22]. Crystals of *Rc*H′f H54N belonged to the cubic space group *F*432, with the unit cell parameter $a \sim 184$ Å, varying slightly among the different crystals. The crystal unit cell contains four *Rc*H′f H54N 24-mers each of them sitting on one of the four special positions of multiplicity 24 of space group *F*432. Hence, the crystal asymmetric unit contains only one protein subunit and the complete quaternary structure of the ferritin cage is obtained by applying the space group symmetry operators. Data collection and processing statistics are displayed in Table 1.

Initial models were obtained by molecular replacement using the software Molrep [23] and one subunit of *Rc*H′f (PDB: 4LQH [9]), excluding non-protein atoms and solvent molecules as searching model. Structural models were refined using the program Refmac5 [24] from the CCP4 suite [22] and a protocol relying on iterative manual rebuilding and maximum-likelihood refinement. The molecular graphics software Coot [25,26] resulted very useful for manual rebuilding and modelling of missing atoms into the electron density. Water molecules were added automatically using the program ARP/wARP [27]. Full three-wavelength anomalous data were collected on the same crystal at remote high energy, peak of the Fe *K*-edge and immediately below the Fe K-edge (specific wavelength used for data collections are reported in Table 1) to provide unambiguous proof that we are observing iron ions. The positions of metal ions were determined from the anomalous Fourier difference maps calculated through FFT [28] from the CCP4 suite. The anomalous signals corresponding to iron ions ranged from 5 σ to 37 σ in the anomalous difference maps computed from data collected at the peak of the Fe *K*-edge. Occupancies of metal ions were estimated according to a criterion based on keeping atomic displacement parameters closed to those of surrounding protein atoms in fully occupied sites. Water molecules bound to metal ions were refined using the same occupancy estimated for the parent metal ion. In the final cycles of refinement all atoms were refined anisotropically except for those residues modeled in multiple conformations or with partial occupancies. Hydrogen atoms were added in calculated positions. Final models were inspected manually and checked with Coot and Procheck [26,29]. Structure solutions and refinement statistics are reported in Table 2. Figures were generated through the molecular graphic software CCP4mg [30].

2.6. Protein Data Bank codes

Final coordinates and structure factors were deposited in the Protein Data Bank (PDB) under the accession codes 6I9P (*Rc*H′f variant H54N), 6I9T (*Rc*H′f H54N – Fe(II) 2 min), 6IAF (*Rc*H′f H54N – Fe(II) 15 min), and 6IAJ (*Rc*H′f H54N – Fe(II) 60 min).

3. Results

3.1. Overall structure of RcH′f variant H54N

A series of structures of *Rc*H′f H54N were obtained through an established protocol relying on time-lapse crystallography [9,10] that allowed us to describe the time evolution of the iron binding events in this ferritin variant. Crystals of iron-free *Rc*H′f H54N were exposed under aerobic conditions to crystalline ferrous ammonium sulphate allowing free iron diffusion into the crystals that were frozen sequentially after 2, 15, and 60 minute exposure.

The ferritin chain was fully traced in all models apart for the starting N-terminal methionine and some of the last C-terminal residues. The crystal asymmetric unit includes a single ferritin subunit representing the spatial and time average of all subunits in the crystal. Both the gel filtration experiment performed during protein purification and the crystal structure demonstrate that *Rc*H′f H54N maintains the quaternary structure of ferritins characterized by a hollow cage resulting from the self-assembling of 24 subunits.

Fig. 1 shows the fold of one *Rc*H′f H54N subunit together with the location of the ferroxidase site and the 3- and 4-fold channels piercing the ferritin cage.

The structures presented in this work include a variable number and type of metal ions (Mg(II) ions from the crystallization buffer and/or Fe (II)/(III) ions from free diffusion). Mg(II) can be distinguished from iron ions according to the detected X-ray anomalous signal. Figs. SI-1A–D and 2A–D report the electron density and the metal ion coordination environments, respectively, in the *Rc*H′f H54N ferroxidase site for iron free (A), 2- (B), 15- (C) and 60- (D) minutes exposure to Fe(II) ions.

3.2. Crystal structure of RcH′f H54N in the iron-free state

In *Rc*H′f H54N five Mg(II) ions are bound in the surroundings of the ferroxidase site with partial occupancy (Figs. SI-1A and 2A). Two of them (Mg2 and Mg3-A) are at the same sites already observed in previous *Rc*H′f structures [9,31,32]. The positions occupied by the couples Mg1- Mg2, Mg1-Mg3A, Mg3-A and Mg3-B are mutually exclusive as their coordination spheres lie far below contact distances. Mg1, observed in both *Rc*H′f H54N/Q variants, but not in *Rc*H′f, is bound at the

Table 1
Data collection and processing. Values for the outer shell are given in parentheses.

	*Rc*H′f – H54N iron free	*Rc*H′f – H54N + Fe(II) 2 min		
PDB code	6I9P	6I9T		
Diffraction source	ESRF BM14	ESRF BM14	Elettra XRD1	Elettra XRD1
Wavelength (Å)	0.8865	0.95372	1.73893	1.76116
Temperature (K)	100	100	100	100
Detector	MARmosaic 225	MARmosaic 225	Pilatus 2M	Pilatus 2M
Crystal-detector distance (mm)	120.0	119.3	100.0	100.0
Rotation range per image (°)	0.50	0.50	0.50	0.50
Total rotation range (°)	60	60	60	60
Exposure time per image (s)	3	3	15.6	15.6
Space group	*F*432	*F*432	*F*432	*F*432
No. of subunit in asymmetric unit	1	1	1	1
a, *b*, *c* (Å)	183.91	183.83	184.21	184.19
Mosaicity (°)	0.30	0.63	0.16	0.22
Resolution range (Å)	21.24–1.25 (1.32–1.25)	22.46–1.20 (1.26–1.20)	42.26–1.70 (1.79–1.70)	46.05–1.85 (1.95–1.85)
Total No. of reflections	1,039,210 (142455)	870,447 (61437)	285,826 (8324)	174,528 (17675)
No. of unique reflections	73,567 (10565)	80,466 (11066)	28,977 (3347)	23,194 (3165)
Completeness (%)	100.0 (100.0)	97.2 (92.9)	96.7 (79.0)	99.1 (95.5)
Anomalous completeness (%)	100.0 (100.0)	95.5 (89.7)	93.3 (58.7)	98.2 (90.1)
Redundancy	14.1 (13.5)	10.8 (5.6)	9.9 (2.5)	7.5 (5.6)
Anomalous redundancy	7.3 (6.8)	5.7 (2.9)	5.3 (1.5)	4.0 (3.0)
$\langle I/\sigma(I)\rangle$	19.1 (6.2)	19.2 (4.0)	23.7 (3.1)	13.9 (2.1)
R_{meas}	0.079 (0.450)	0.063 (0.452)	0.066 (0.315)	0.113 (0.854)
Overall *B* factor from Wilson plot (Å^2)	9.1	5.7	8.8	9.6

	*Rc*H′f – H54N + Fe(II) 15 min			*Rc*H′f – H54N + Fe(II) 60 min
PDB code	6IAF			6IAJ
Diffraction source	ESRF BM14	Elettra XRD1	Elettra XRD1	ESRF BM14
Wavelength (Å)	0.95372	1.73893	1.76116	0.95372
Temperature (K)	100	100	100	100
Detector	MARmosaic 225	Pilatus 2 M	Pilatus 2 M	MARmosaic 225
Crystal-detector distance (mm)	119.3	100.0	100.0	133.6
Rotation range per image (°)	0.50	0.50	0.50	0.50
Total rotation range (°)	60	50	50	60
Exposure time per image (s)	4	12.5	12.5	4
Space group	*F*432	*F*432	*F*432	*F*432
No. of subunit in asymmetric unit	1	1	1	1
a, *b*, *c* (Å)	183.72	183.66	183.35	184.13
Mosaicity (°)	0.32	0.18	0.23	0.69
Resolution range (Å)	22.44–1.35 (1.42–1.35)	45.92–1.78 (1.88–1.78)	42.06–2.34 (2.47–2.34)	24.60–1.62 (1.71–1.62)
Total No. of reflections	830,491 (115586)	231,378 (16882)	114,534 (16879)	269,475 (31565)
No. of unique reflections	58,512 (8388)	25,933 (3637)	11,677 (1656)	34,490 (4928)
Completeness (%)	100.0 (100.0)	99.8 (99.0)	100.0 (100.0)	100.0 (100.0)
Anomalous Completeness (%)	100.0 (100.0)	99.1 (94.4)	100.0 (100.0)	100.0 (100.0)
Redundancy	14.2 (13.8)	8.9 (4.6)	9.8 (10.2)	7.8 (6.4)
Anomalous Redundancy	7.4 (7.0)	4.7 (2.5)	5.3 (5.4)	4.1 (3.3)
$\langle I/\sigma(I)\rangle$	22.3 (6.0)	12.4 (2.0)	7.3 (3.5)	9.6 (2.8)
R_{meas}	0.078 (0.480)	0.129 (0.680)	0.190 (0.822)	0.130 (0.463)
Overall *B* factor from Wilson plot (Å^2)	9.9	7.4	8.0	7.8

Fe1 site. The remaining Mg(II) ions are bound to other locations in the vicinity of the ferroxidase site. In all structures and mainly in *Rc*H′f H54N, the metal-coordinating residues in the surroundings of the catalytic cavity display conformational disorder, indicating non-specific binding and fluxional behavior. As in the other ferritin structures [9,10,32], the three-fold channel is occupied by two magnesium hexa-aqua ions (Fig. SI-2A).

3.3. Crystal structure of RcH′f H54N after 2 minute iron diffusion

The structure obtained after 2 min of free iron diffusion under aerobic conditions was refined to 1.20 Å resolution. A detailed analysis of the anomalous difference Fourier maps computed from data collected at the peak of the Fe K-edge and immediately below the metal edge reveals that the first iron binding event occurring in the ferroxidase site is the population of the Fe1 site as indicated by the strong anomalous signal (22 σ) present in the map (Fig. SI-1B). The occupancy of Fe1 by iron has been estimated to 40%. The Fe1 coordination geometry is the already observed quite regular square pyramid having the carboxylate oxygens of Glu23 and Glu58 and two water molecules in the basal plane and His61 Nδ in the apex [9,10] (Fig. 2B). Three magnesium ions are still observed within the ferroxidase cavity, complicating the interpretation of the electron density. Similarly, after 2 min of exposure to iron ions of the *Rc*H′f H54Q variant [9], the only site occupied is Fe1 displaying the same square-pyramidal coordination. *Rc*H′f H54N and *Rc*H′f H54Q appear to behave differently with respect to *Rc*H′f where both Fe1 and Fe2 sites are already occupied by Fe ions after 2 min with a 30% occupancy [9]. Mg(II) hexa-aqua ions are present in the three-fold channels where they establish second sphere interactions with the side chains of Asp127, Glu130 and Ser131.

3.4. Crystal structure of RcH′f H54N after 15 minute iron diffusion

The structure of *Rc*H′f H54N determined after 15 min of free iron

Table 2
Structure solution and refinement. Values for the outer shell are given in parentheses.

	*Rc*H′f – H54N iron free	*Rc*H′f – H54N + Fe(II)		
		2 min	15 min	60 min
PDB code	6I9P	6I9T	6IAF	6IAJ
Resolution range (Å)	21.10–1.25 (1.28–1.25)	22.30–1.20 (1.23–1.20)	22.44–1.35 (1.39–1.35)	23.98–1.62 (1.66–1.62)
Completeness (%)	99.91 (99.96)	97.00 (92.62)	99.94 (99.98)	99.89 (100.00)
No. of reflections, working set	69,785 (5020)	76,291 (5316)	55,550 (4038)	32,739 (2364)
No. of reflections, test set	3705 (280)	4142 (278)	2960 (208)	1728 (127)
Final R_{cryst}	0.117 (0.153)	0.121 (0.204)	0.113 (0.158)	0.154 (0.211)
Final R_{free}	0.133 (0.169)	0.137 (0.222)	0.141 (0.165)	0.184 (0.230)
No. of non-H atoms				
Protein	1606	1605	1590	1581
Anions (Cl)	11	9	9	7
Metal ions (Fe, Mg)	14 (0, 14)	14 (1, 13)	14 (7, 7)	13 (7, 6)
Water	392	384	384	349
Total	2023	2012	1997	1950
R.m.s. deviations				
Bonds (Å)	0.009	0.009	0.009	0.009
Angles (°)	1.477	1.519	1.481	1.549
Average *B* factors (Å^2)	10.72	9.78	10.75	13.40
Estimate error on coordinates based on R value (Å)	0.029	0.027	0.035	0.071
Ramachandran plot				
Most favored (%)	98.8	98.8	98.2	98.2
Allowed (%)	1.2	1.2	1.8	1.8

diffusion was refined to 1.35 Å resolution. The analysis of the ferroxidase site reveals that magnesium ions are no longer present in the cavity. The Fe1 site is occupied by an iron ion coordinated by Glu23, Glu58, His61, and water/hydroxide molecules in a quite regular square pyramidal coordination geometry (Figs. SI-1C and 2C). The Fe2 site becomes populated by iron ions, while the occupancy of the Fe1 site still remains at 40%. In Fe2, the signal in the anomalous difference Fourier map is broadened over two close positions (distance ~1.5 Å) in which iron has been modeled at partial occupancy (40% and 60%, respectively), corresponding to two mutually exclusive sites, named Fe2-A and Fe2-B (Fig. SI-1C). The position of Fe2-A perfectly matches the canonical Fe2 site in which iron is coordinated by Glu58 (monodentate), Glu103 (bidentate, A-conformation), and a water/hydroxide molecule, Wb, that together with Glu58 bridges the two iron ions in the ferroxidase site. Wb is located 2.04 ± 0.05 and 1.87 ± 0.05 Å away from Fe1 and Fe2-A, respectively. Instead, Fe2-B is coordinated by Glu103 (B-conformation), Asp140 (monodentate), Gln137 (monodentate) and three water molecules in a quite regular octahedral coordination geometry (Fig. 2C). The Fe1 - Fe2-A distance is 3.58 ± 0.05, while the Fe1 – Fe2-B distance is 4.09 ± 0.05 Å. A

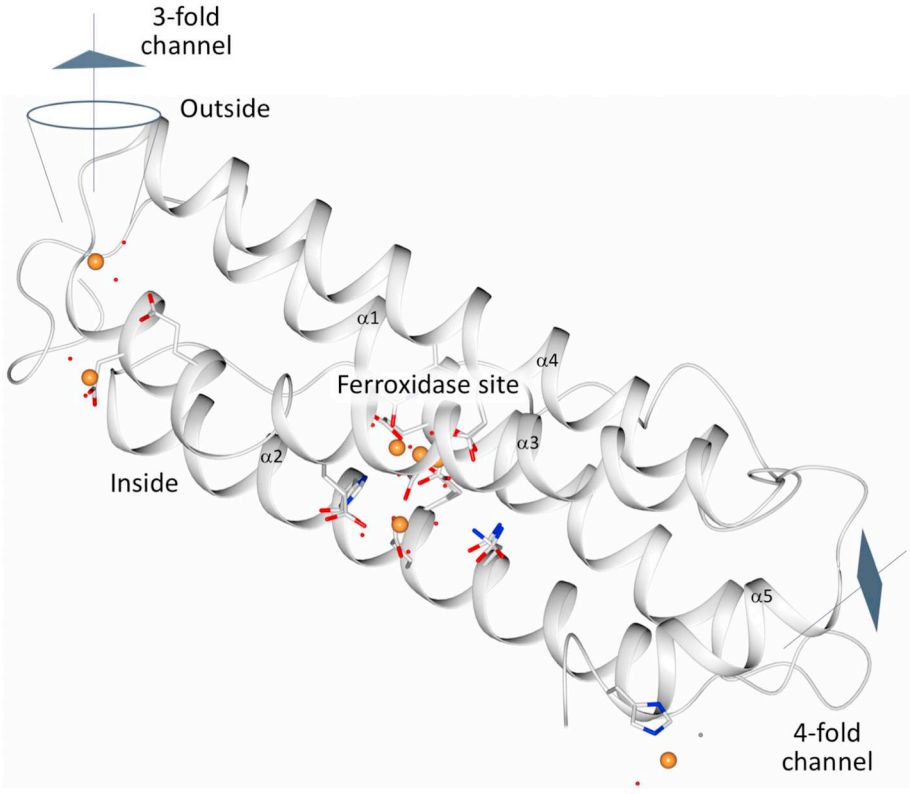

Fig. 1. Subunit of the RcH′f variant H54N represented as white ribbon (the five α-helices are sequentially numbered from the N-terminus). The ferroxidase site is highlighted by the presence of iron ions (orange spheres of arbitrary radius), coordinated to residues (in sticks, white carbons) and water molecules (red spheres). The three-fold and the four-fold channels are indicated (iron ions and meaningful residues inside the channels are shown). Oxygen and nitrogen atoms are colored red and blue, respectively. Water molecules and chloride anions are shown as red and grey spheres, respectively.

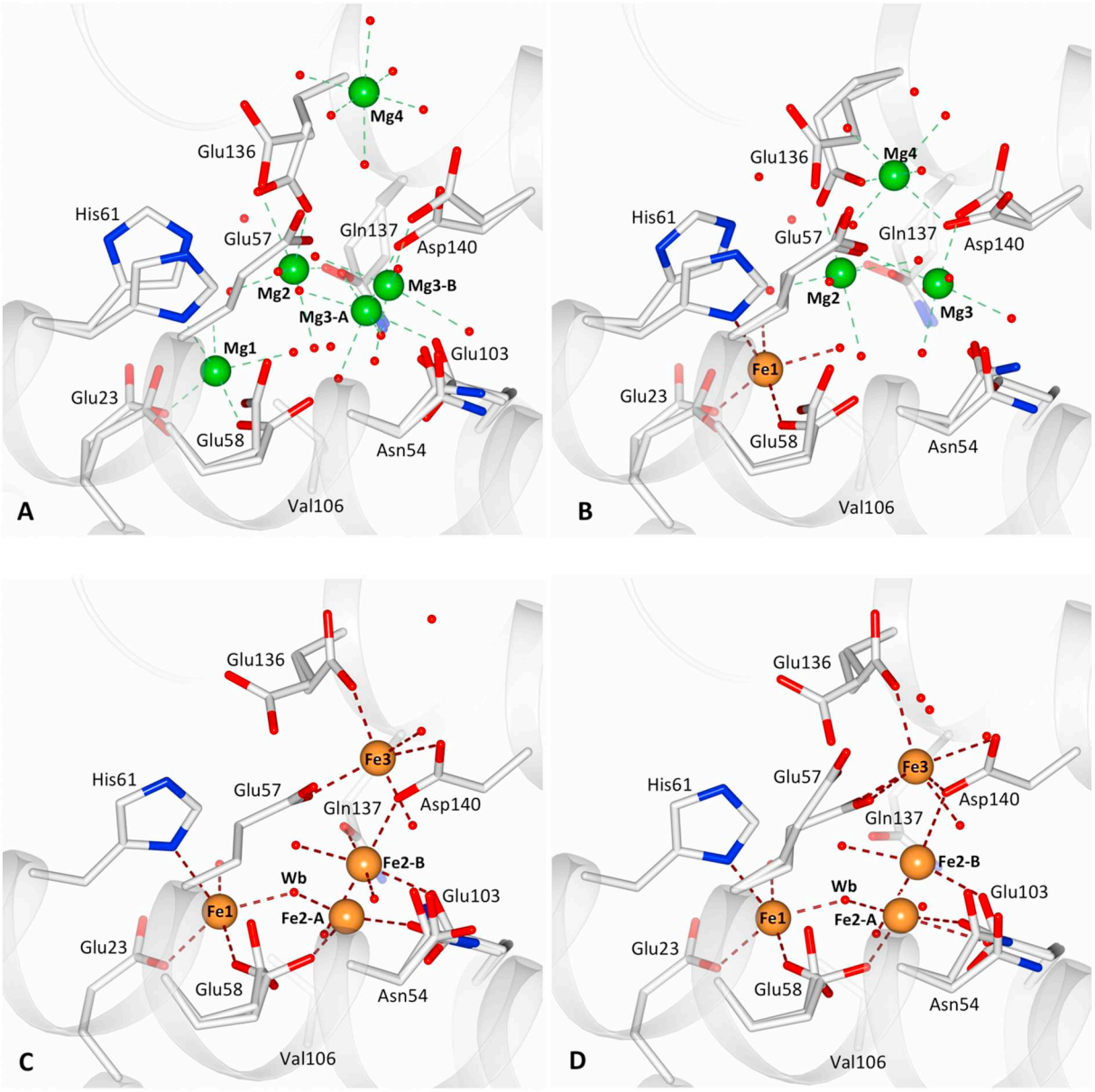

Fig. 2. Ferroxidase site view of RcH′f variant H54N in the iron free-state (A panel) and after 2 (B panel), 15 (C panel), and 60 (D panel) minutes of free iron diffusion. Coordination bonds for iron (orange spheres) and magnesium (green spheres) ions are displayed as dark red and green dashed lines, respectively. Only magnesium ions, raising from the crystallization solution, are found in the ferroxidase site in the iron-free state (A panel). After 2 min of iron exposure (B panel) the ferroxidase site 1 becomes populated by iron ions whereas residual magnesium ions are still present inside the catalytic cavity. The gain of the iron exposure time to 15 (C panel) and 60 (D panel) minutes results in iron ions populating the ferroxidase site. Two alternate positions are observed for Fe2: the first, Fe2-A, corresponds to the canonical position of the ferroxidase site 2, whereas the second, Fe2-B, represents a position never observed in RcH′f. Fe1 and Fe2-A are bridged by a water/hydroxo species (Wb, red sphere). Water molecules are displayed as red spheres, oxygens are colored red and nitrogens blue.

further iron ion, named Fe3 (70% occupancy), coordinated by Glu57 (bidentate), Glu136 (monodentate), and Asp140 (monodentate) is present in the proximity of the ferroxidase site (Figs. SI-1C and 2C). The octahedral coordination geometry characterizing Fe3 is completed by two water molecules. Fe3 is placed 5.25 ± 0.05 and 4.54 ± 0.05 Å away from Fe2-A and Fe2-B, respectively.

Comparison with the structures of *Rc*H′f and *Rc*H′f H54Q, obtained at the same times of iron salt diffusion, shows a different behavior (Fig. 3A–C). *Rc*H′f hosts four iron ions in the ferroxidase site and surrounding space [9]. Fe1 and Fe2 are occupied at 70%. Fe1 and Fe2 match the positions of Fe1 and Fe2-A of *Rc*H′f H54N with the same coordination geometry. Fe3, bound to His54 in *Rc*H′f, is obviously missing in *Rc*H′f H54N, while Fe4 is the same as Fe3 of *Rc*H′f H54N. Fe2B of *Rc*H′f H54N is missing in *Rc*H′f. In *Rc*H′f H54Q, five iron ions are present in the ferroxidase site and surroundings. The Fe1, Fe2A and Fe3 sites of *Rc*H′f H54N correspond to *Rc*H′f H54Q sites Fe1, Fe2 and Fe4. The remaining two iron ions of *Rc*H′f H54Q, Fe3 and Fe5, that involve the binding to Gln54, are not observed in *Rc*H′f H54N.

Two hexa-aqua iron ions, named Fe5 and Fe6, occupy the three-fold channels of *Rc*H′f H54N (Fig. SI-2B). These are located deeply inside the channel (~11.0 and ~18.0 Å from the protein surface), where they entail a network of H-bonds, mediated by their water ligands, with the side chains of Asp127, Glu130 and Ser131. The occupancies for Fe5 and Fe6 in this site have been estimated to 75% and 60%, respectively. A Mg(II) hexa-aqua ion is present on the external part of the channel (Fig. SI-2B). A six-coordinated iron ion (Fe7) fully occupies the four-fold axis channel bound to the Nε of four symmetry-related His169 in a plane, to a water molecule, on the internal side of the pore, and a chloride anion,

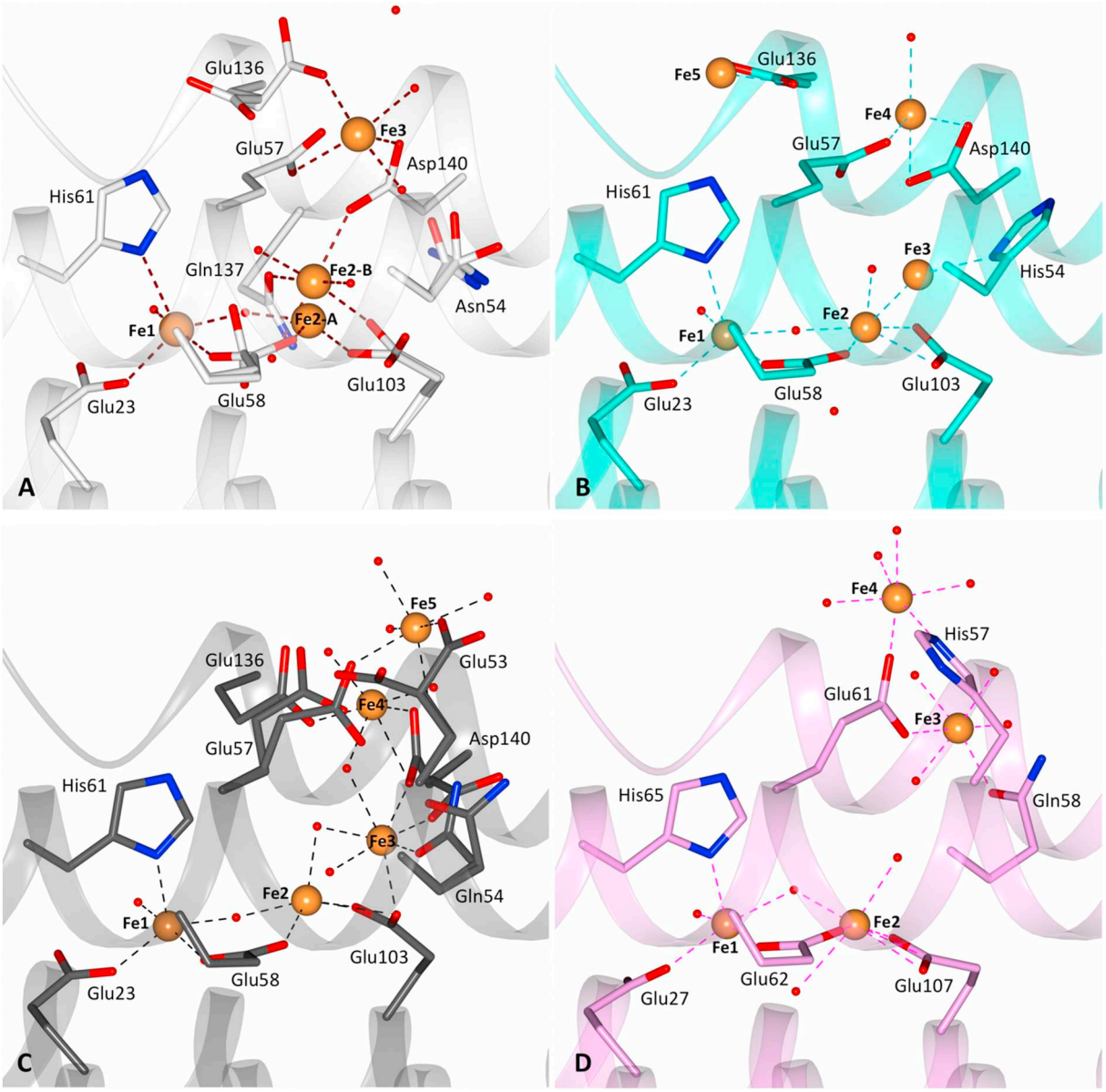

Fig. 3. Ferroxidase site view showing iron ions (orange spheres) bound to A) *Rc*H′f variant H54N (white cartoon and carbon atoms, iron coordination is displayed as dark red dashed lines; PDB id 6IAF), B) *Rc*H′f (cyan cartoon and carbons, iron coordination as cyan dashed lines; PDB id 4LYU) [9], C) *Rc*H′f variant H54Q (dark grey cartoon and carbons, iron coordination as dark grey dashed lines; PDB id 4MN9) [9], and D) HuHf (pink cartoon and carbons, iron coordination as pink dashed lines, PDB id 4OYN) [10]. The four panels report ferritin structures determined at the same iron exposure time of 15 min.

on the outside (Fig. SI-3).

3.5. Crystal structure of RcH′f H54N after 60 minutes iron diffusion

The structure of *Rc*H′f H54N determined after 60 minute iron exposure was refined to 1.62 Å resolution. The conformation of the active site and the positions occupied by iron ions inside the ferroxidase site and surroundings, closely resemble those described for the structure determined after 15 min of free-iron diffusion. Fe1 (40% occupancy) is coordinated by Glu23, His61, Glu58, a water molecule and the water/hydroxide species, Wb, in a square pyramidal geometry (Figs. SI-1D and 2D). Consistently with the structure determined after 15 minute iron-exposure, two alternate positions are observed for Fe2 (almost perfectly matching those already described). The Fe2-A and Fe2-B, whose occupancies have been estimated to 40% and 60%, are located 3.62 ± 0.10 and 4.17 ± 0.10 Å away from Fe1, respectively. As in the 15 minute structure, Fe3 is bound in the same coordination environment. The occupancy in this site has been estimated to 70% and distances of 4.89 ± 0.10 and 4.20 ± 0.10 Å separate Fe3 from Fe2-A and Fe2-B, respectively.

Iron ions occupy exactly the same positions inside three-fold and four-fold channels identified after 15 minutes of free-iron diffusion (Figs. SI-2B and SI-3).

The structure of *Rc*H′f determined after 60 min of iron salt diffusion shows the Fe1 and Fe2 sites occupied by Fe ions at the same occupancy of those found in *Rc*H′f H54N [9]. The Fe1 and Fe2 sites have also been observed in 60 min *Rc*H′f H54Q, but with occupancy of 80% for Fe1 and 40% for Fe2 [9].

3.6. Kinetic studies

Fig. 4 compares the stopped-flow kinetic measurements for wt *Rc*H′f and its H54Q and H54N variants, recorded after addition of 2 Fe^{2+}/ subunit. The growth and decay of the 650 nm absorbance is diagnostic

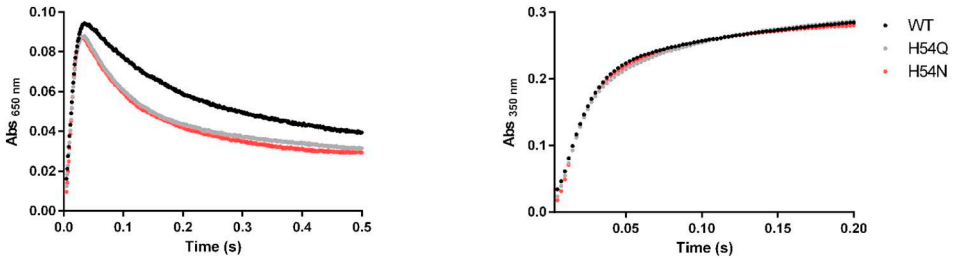

Fig. 4. UV/Vis spectroscopic analysis of the ferroxidase activity under rapid mixing. Formation of DFP intermediate (A650 [nm]; left) and ferric products (A350 [nm]; right) measured after the addition of Fe^{2+}/subunit (2:1) in *Rc*H′f (WT, black dots), *Rc*H′f H54Q (H54Q, grey dots) and *Rc*H′f H54N (H54N, red dots). Each curve represents the average of three measurements.

for the formation and disappearance of the DFP intermediate, while the absorbance at 350 nm shows the formation of the ferric products. The curves for the H54Q and H54N are essentially superimposable one with another. Small differences are observed with respect to the wild-type protein, in particular as far as the decay rate of the DFP species is concerned, which appears to be slightly faster in the two mutants. A similar effect was observed for H54A under the same iron stoichiometry.

4. Discussion

4.1. Time-lapse iron uptake in crystals

The results on H54N confirm the same general trend in the progressive population of transient iron binding sites, with some minor but significant differences in the accessory iron binding sites, with respect to *Rc*H′f and *Rc*H′fH54Q, as detailed below.

The first iron-binding event in *Rc*H′f H54N, detected after 2 min of free iron diffusion, is the population of the Fe1 site. The higher affinity of this site for metal ions was previously outlined by thermodynamic [14,33] and structural [9,10,34] studies on either *Rc*H′f and HuHf. Consistently, a high-affinity iron binding site corresponding to the Fe1 site in *Rc*H′f was also reported in the structures of ferritins from other organisms, such as those of *Pseudo-nitzschia multiseries* [35,36], *Escherichia coli* [37] and *Pyrococcus furiosus* [38]. In *Rc*H′f H54N, the Fe1 site is still populated on extending iron exposure time to 15 and 60 min. However, its population does not increase with time, remaining constant at about 40%. After 15 min of iron diffusion, we observe two close, mutually excluding, positions for iron bound to the sites named Fe2-A and Fe2-B (Figs. SI-1C and 3C).

In the catalytic center, the Fe1 and Fe2-A ions are bridged by Glu58 (A conformation) on one side and by the water/hydroxide (Wb) molecule on the other, as already observed in *Rc*H′f [9]. The comparison between the structures of the H54N variant and those of the wt-enzyme (determined under the same conditions) shows only minor differences in the placement of this bridging species.

The Fe1 - Fe2-A distance in the H54N variant is the same after 15 and 60 minute iron exposure, (3.58 ± 0.05 Å vs. 3.62 ± 0.10 Å). Previous structural analysis performed on the *Rc*H′f consistently reported Fe1 - Fe2 distances ranging from 3.54 to 3.76 Å at pH ~8, whereas slightly shorter distances, ranging from 3.49 to 3.52 Å, were measured in HuHf under the same experimental conditions [9,10]. On the other hand, studies performed on *Rc*H′f using crystals grown at pH 6.5, revealed a shorter Fe1 – Fe2 distance, ~3.15 Å [9,31]. Analysis of the intermetallic distances in the structures of *Rc*H′f pointed out that different catalytic stages were characterized in the ferroxidase site. Diferrous clusters populated Fe1 and Fe2 sites at higher pH value, whereas μ-oxo/μ-hydroxo ferric clusters were observed at pH to 6.5. On the contrary, for HuHf a mixed-valence model was proposed [10]. These observations were in agreement with the reported pH dependence of Fe(II) oxidation kinetics determined for *Rc*H′f (and variants), showing an increase by ~100 times in the formation rate of diferric products and DFP intermediate in raising the pH from 6.0 to 8.0 [39]. According to these data, at slightly acidic pH the rate-limiting steps are the formation and the release of the diferric product from the ferroxidase site, leading to their direct observation in crystals exposed to iron ions. On the contrary, the higher turnover rate occurring at higher pH makes the binding of iron ions at the Fe1 and Fe2 sites the slowest step of the reaction leading to the characterization of di-ferrous iron clusters in the ferroxidase site. Further evidence in support of the presence of Fe(II) clusters at pH ~8 was provided by the structural characterization of *Rc*H′f iron-loaded under strict anaerobic conditions [9]. The di-ferrous clusters, formed in absence of the second substrate O_2 (PDB: 4MY7), displayed a Fe1 - Fe2 distance of 3.64 ± 0.08 Å, the same measured in this H54N variant.

The structures of *Rc*H′f H54N determined after 15 and 60 min of iron exposure revealed the presence of an additional iron ion, Fe3, anchored to Glu57, Glu136 and Asp140.

We have previously shown that, when the amino acids responsible for iron shuttling towards the ferroxidase site, mainly Glu57, Glu136 and Asp140 in *Rc*H′f, are changed into alanines (*Rc*H′f variant E57A-E136A-D140A), the enzyme retains its ability to bind iron ions in the ferroxidase site (with unaltered coordination geometry) but the reaction turnover is drastically impaired making this variant almost unable to process Fe(II) ions on the ms time scale [11]. The position of Fe3 identified in *Rc*H′f H54N structurally matches the so-called Fe4 in the structures of the native enzyme and in the H54Q variant (determined after the same iron exposure time). The Fe3 site, involving residue 54, observed in *Rc*H′f and in *Rc*H′f H54Q is missing in *Rc*H′f H54N (Fig. 3A–D). A new iron position, dubbed Fe2-B, and alternative to the occupancy of the “standard” Fe2-A site, has been observed in *Rc*H′f H54N. Here iron is anchored to Glu103, Gln137 and Asp140. Reasonably, the Fe2-B is incoming ferrous ion moving towards the catalytic center and not yet ready to establish the dinuclear site. Fe2-B is positioned ~4.1 Å away from Fe1 (4.09 ± 0.05 Å and 4.17 ± 0.10 Å, respectively) and detected after 15 and up to 60 minute exposure (Figs. SI-1 and 2 panels C and D). The comparison with the structure of the iron-free *Rc*H′f H54N also displays a magnesium ion, named Mg3-A, in the same position occupied by Fe2-B (Figs. 2A, C and SI-1A, C).

Even though iron ions were previously observed in the Fe2 site in both *Rc*H′f and HuHf, to date iron binding in a site corresponding to Fe2-B has never been reported in these enzymes.

Notably, both Gln54 in the H54Q mutant and His54 in *Rc*H′f are directly involved in iron coordination, contributing to shuttle freshly incoming ferrous ions towards the active site. While the iron binding residues in the Fe1 and Fe2 sites are fully conserved among species, the iron shuttling residues are not fully retained, resulting in a variable composition of this portion of the protein. Structural evidences on HuHf proved the involvement of Gln58 in the iron shuttling process, exactly as observed for Gln54 in *Rc*H′f H54Q (representing a ‘humanized’ form of the frog protein) [9,10]. Reviewing all structures determined so far, we have seen that His54 (in *Rc*H′f), Gln54 (in *Rc*H′f H54Q), Gln58 (in HuHf) are directly involved in binding iron ions approaching the catalytic site. Fig. 3A–D shows the different iron binding sites observed by X-ray crystallography in *Rc*H′f H54N (3A), *Rc*H′f (3B), *Rc*H′f H54Q (3C) and HuHf (3D). Native His54 (in *Rc*H′f), Gln58 (in HuHf) and Gln54 (in *Rc*H′f H54Q), all contribute to establish transient iron binding sites together with other residues in the surroundings of the catalytic site. Only Asn54, due to its shorter side chain cannot contribute to establish a proper metal coordination site, stable enough to allow the detection of

a metal-N54 bond. This does not mean that Asn54 cannot interact at all with incoming iron ions; instead, it favors the formation of the novel binding site Fe2-B.

The Fe7 observed in the four-fold channels (Fig. SI-3), deserves a separate comment. The Fe7 bound to four symmetry-related His169, as already observed in *Rc*H′f [9], does not seem to play any role in the biomineralization reaction. The ferroxidase activity in the H169F variant is indeed unaffected [40]. The transit of cations through the four-fold channel is hindered by a high energetic barrier due to its hydrophobic nature [15]. Only by engineering these channels to create attractive electric gradients, they become permeable to cations [13]. The functional role of the four-fold channels in animal ferritins needs to be further investigated.

4.2. Solution kinetics

The stopped-flow kinetic measurements on *Rc*H′f H54N show the standard behavior of *Rc*H′f and HuHf, with a fast formation and decay of the diferric peroxo intermediate and formation of ferric products (Fig. 4). The only meaningful difference observed between *Rc*H′f and its two H54Q and H54N variants is a slightly faster decay of the DFP intermediate. The effects are smoother than what observed for the *Rc*H′f H54A variant where, with the same stoichiometry of $2Fe^{2+}$/subunit the faster decay of the intermediate was accompanied by a slightly faster formation of the intermediate and of the final ferric products [12]. These effects are by far weaker than those observed by replacing with Ala the negatively charged residues in the accessory iron binding sites where the ability of impairing the iron oxidation on the ms time scales increases in the order E136A < E57A < E57AE136A ≪ E57AE136AD140A [11], thus further demonstrating the dominant role for iron uptake of carboxylates and electrostatic gradients along the iron paths [13].

5. Conclusions

Over the years we have developed an approach aimed at defining the mechanism of iron uptake in eukaryotic ferritins [5,9–11,31]. Flash-freezing ferritin crystals at different time intervals after exposure to a ferrous salt, allows us follow iron uptake by the ferritin cage along a backward path where the first sites to be populated are those in the ferroxidase center, followed by accessory sites at the interface between the ferroxidase center and the inner cavity and finally the ion entry channels. Iron accumulates at transiently and weakly coordinating sites distributed along this path because of the hindered turnover in the crystal. The functional relevance of these sites is validated by measuring the reaction efficiency in solution in ferritin variants produced upon mutation of amino acids observed to act as iron ligands. The role played by His54, one of the residues contributing to accessory sites [9,11], is here further investigated by means of the kinetic and crystallographic characterization of the H54N variant.

The set of high-resolution crystal structure presented here highlights the changes in metal ion distribution in *Rc*H′f occurring upon mutation of His54 into Asn. Comparison with the structures and kinetic behavior of *Rc*H′f, HuHf and other mutants of *Rc*H′f at position 54, indicate the specific function of this residue in iron processing by ferritin. Previous kinetic studies suggested that His54 acts as an ion trap to ensure a proper access of iron ions to the ferroxidase site [12]. Substitution of His54 by Gln maintains such function, whereas substitution with Asn abolishes the direct binding to iron ions, although it does not prevent the presence a transient coordination site for iron ions in the close proximity of the ferroxidase site. The detection of the Fe site 2-B in the structure of *Rc*H′f H54N show that Asn at position 54 induces a slight change in the pathway leading incoming Fe(II) ions to the catalytic site.

Therefore, as long as a path of accessory iron binding sites exist, the catalytic iron oxidation reaction via the diferric peroxo intermediate can take place on its typical ms time scale, although with slightly modified kinetics.

Abbreviations

*Rc*H′f	*Rana catesbeiana* ferritin heavy subunit
HuHf	human ferritin heavy chain
PCR	polymerase chain reaction
IPTG	isopropyl-β-D-1-thiogalactopyranoside
PDB	Protein Data Bank
SDS-PAGE	sodium dodecyl sulphate - polyacrylamide gel electrophoresis
DFP	diferric-peroxo
wt	wild-type

Acknowledgments

We would like to thank the European Synchrotron Radiation Facility (ESRF) and the Elettra Synchrotron for providing us beamtime, and the staff of beamlines BM14 (ESRF) and XRD1 (Elettra) for their assistance during the experimental sessions. The authors acknowledge the support and the use of resources of Instruct-ERIC, a Landmark ESFRI project, and specifically the CERM/CIRMMP Italy Centre.

Appendix A. Supplementary data

Supplementary data to this article can be found online at https://doi.org/10.1016/j.jinorgbio.2019.110697.

References

[1] E.C. Theil, R.K. Behera, T. Tosha, Coord. Chem. Rev. 257 (2013) 579–586, https://doi.org/10.1016/j.ccr.2012.05.013.
[2] C. Bernacchioni, V. Ghini, C. Pozzi, P.F. Di, E.C. Theil, P. Turano, ACS Chem. Biol. 9 (2014) 2517–2525, https://doi.org/10.1021/cb500431r.
[3] E.C. Theil, Curr. Opin. Chem. Biol. 15 (2011) 304–311, https://doi.org/10.1016/j.cbpa.2011.01.004.
[4] P. Arosio, T.G. Adelman, J.W. Drysdale, J. Biol. Chem. 253 (1978) 4451–4458.
[5] C. Pozzi, S. Ciambellotti, C. Bernacchioni, F. Di Pisa, S. Mangani, P. Turano, Proc. Natl. Acad. Sci. 114 (2017) 2580–2585, https://doi.org/10.1073/pnas.1614302114.
[6] T. Tosha, M.R. Hasan, E.C. Theil, Proc. Natl. Acad. Sci. U. S. A. 105 (2008) 18182–18187, https://doi.org/10.1073/pnas.0805083105.
[7] A. Treffry, E.R. Bauminger, D. Hechel, N.W. Hodson, I. Nowik, S.J. Yewdall, P.M. Harrison, Biochem. J. 296 (Pt 3) (1993) 721–728.
[8] R.K. Behera, R. Torres, T. Tosha, J.M. Bradley, C.W. Goulding, E.C. Theil, J. Biol. Inorg. Chem. 20 (2015) 957–969, https://doi.org/10.1007/s00775-015-1279-x.
[9] C. Pozzi, P.F. Di, D. Lalli, C. Rosa, E. Theil, P. Turano, S. Mangani, F. Di Pisa, D. Lalli, C. Rosa, E. Theil, P. Turano, S. Mangani, Acta Crystallogr. D Biol. Crystallogr. 71 (2015) 941–953, https://doi.org/10.1107/S1399004715002333.
[10] C. Pozzi, F. Di Pisa, C. Bernacchioni, S. Ciambellotti, P. Turano, S. Mangani, Acta Crystallogr. D Biol. Crystallogr. 71 (2015) 1909–1920, https://doi.org/10.1107/S1399004715013073.
[11] C. Bernacchioni, C. Pozzi, F. Di Pisa, S. Mangani, P. Turano, Chem. Eur. J. 22 (2016) 16213–16219, https://doi.org/10.1002/chem.201602842.
[12] C. Bernacchioni, S. Ciambellotti, E.C. Theil, P. Turano, Biochim. Biophys. Acta 1854 (2015) 1118–1122, https://doi.org/10.1016/j.bbapap.2015.02.011.
[13] C. Bernacchioni, V. Ghini, E.C. Theil, P. Turano, RSC Adv. 6 (2016) 21219–21227, https://doi.org/10.1039/C5RA25056K.
[14] F. Bou-Abdallah, P. Arosio, P. Santambrogio, X. Yang, C. Janus-Chandler, N.D. Chasteen, Biochemistry 41 (2002) 11184–11191.
[15] B. Chandramouli, C. Bernacchioni, D. Di Maio, P. Turano, G. Brancato, J. Biol. Chem. 291 (2016) 25617–25628, https://doi.org/10.1074/jbc.M116.748046.
[16] R.K. Behera, E.C. Theil, Proc. Natl. Acad. Sci. 111 (2014) 7925–7930, https://doi.org/10.1073/pnas.1318417111.
[17] O.M.H.M. Salo-Ahen, A. Tochowicz, C. Pozzi, D. Cardinale, S. Ferrari, Y. Boum, S. Mangani, R.M.M. Stroud, P. Saxena, H. Myllykallio, M.P.P. Costi, G. Ponterini, R.C.C. Wade, J. Med. Chem. 58 (2015) 3572–3581, https://doi.org/10.1021/acs.jmedchem.5b00137.
[18] P. Turano, D. Lalli, I.C. Felli, E.C. Theil, I. Bertini, Proc. Natl. Acad. Sci. U. S. A. 107 (2010) 545–550, https://doi.org/10.1073/pnas.0908082106.
[19] H.R. Powell, O. Johnson, A.G.W. Leslie, Acta Crystallogr. D Biol. Crystallogr. 69 (2013) 1195–1203, https://doi.org/10.1107/S0907444912048524.
[20] W. Kabsch, Acta Crystallogr. D Biol. Crystallogr. 66 (2010) 125–132, https://doi.org/10.1107/S0907444909047337.
[21] P. Evans, Acta Crystallogr. D Biol. Crystallogr. 62 (2006) 72–82, https://doi.org/10.1107/S0907444905036693.
[22] M.D. Winn, C.C. Ballard, K.D. Cowtan, E.J. Dodson, P. Emsley, P.R. Evans, R.M. Keegan, E.B. Krissinel, A.G.W. Leslie, A. McCoy, S.J. McNicholas, G.N. Murshudov, N.S. Pannu, E.A. Potterton, H.R. Powell, R.J. Read, A. Vagin,

K.S. Wilson, Acta Crystallogr. D Biol. Crystallogr. 67 (2011) 235–242, https://doi.org/10.1107/S0907444910045749.
[23] A. Vagin, A. Teplyakov, Acta Crystallogr. D Biol. Crystallogr. 66 (2010) 22–25, https://doi.org/10.1107/S0907444909042589.
[24] G.N. Murshudov, P. Skubák, A.A. Lebedev, N.S. Pannu, R.A. Steiner, R.A. Nicholls, M.D. Winn, F. Long, A.A. Vagin, Acta Crystallogr. D Biol. Crystallogr. 67 (2011) 355–367, https://doi.org/10.1107/S0907444911001314.
[25] P. Emsley, K. Cowtan, Acta Crystallogr. D Biol. Crystallogr. 60 (2004) 2126–2132, https://doi.org/10.1107/S0907444904019158.
[26] P. Emsley, B. Lohkamp, W.G. Scott, K. Cowtan, Acta Crystallogr. D Biol. Crystallogr. 66 (2010) 486–501, https://doi.org/10.1107/S0907444910007493.
[27] G. Langer, S.X. Cohen, V.S. Lamzin, A. Perrakis, Nat. Protoc. 3 (2008) 1171–1179, https://doi.org/10.1038/nprot.2008.91.
[28] R.J. Read, A.J. Schierbeek, J. Appl. Crystallogr. 21 (1988) 490–495, https://doi.org/10.1107/S002188988800562X.
[29] R.A. Laskowski, M.W. MacArthur, J.M. Thornton, Curr. Opin. Struct. Biol. 8 (1998) 631–639.
[30] S. McNicholas, E. Potterton, K.S. Wilson, M.E.M. Noble, Acta Crystallogr. D Biol. Crystallogr. 67 (2011) 386–394, https://doi.org/10.1107/S0907444911007281.
[31] I. Bertini, D. Lalli, S. Mangani, C. Pozzi, C. Rosa, E.C. Theil, P. Turano, J. Am. Chem. Soc. 134 (2012) 6169–6176, https://doi.org/10.1021/ja210084n.
[32] T. Tosha, H.L. Ng, O. Bhattasali, T. Alber, E.C. Theil, J. Am. Chem. Soc. 132 (2010) 14562–14569, https://doi.org/10.1021/ja105583d.
[33] F. Bou-Abdallah, P. Arosio, S. Levi, C. Janus-Chandler, N.D. Chasteen, J. Biol. Inorg. Chem. 8 (2003) 489–497, https://doi.org/10.1007/s00775-003-0455-6.
[34] A. Treffry, Z. Zhao, M.A. Quail, J.R. Guest, P.M. Harrison, Biochemistry 36 (1997) 432–441, https://doi.org/10.1021/bi961830l.
[35] A. Marchetti, M.S. Parker, L.P. Moccia, E.O. Lin, A.L. Arrieta, F. Ribalet, M.E.P. Murphy, M.T. Maldonado, E.V. Armbrust, Nature 457 (2009) 467–470, https://doi.org/10.1038/nature07539.
[36] S. Pfaffen, R. Abdulqadir, N.E. Le Brun, M.E.P. Murphy, J. Biol. Chem. 288 (2013) 14917–14925, https://doi.org/10.1074/jbc.M113.454496.
[37] T.J. Stillman, P.D. Hempstead, P.J. Artymiuk, S.C. Andrews, A.J. Hudson, A. Treffry, J.R. Guest, P.M. Harrison, J. Mol. Biol. 307 (2001) 587–603.
[38] J. Tatur, W.R. Hagen, P.M. Matias, J. Biol. Inorg. Chem. 12 (2007) 615–630, https://doi.org/10.1007/s00775-007-0212-3.
[39] X. Liu, E.C. Theil, Proc. Natl. Acad. Sci. 101 (2004) 8557–8562, https://doi.org/10.1073/pnas.0401146101.
[40] E.C. Theil, P. Turano, V. Ghini, M. Allegrozzi, C. Bernacchioni, J. Biol. Inorg. Chem. 19 (2014) 615–622, https://doi.org/10.1007/s00775-014-1103-z.